NUMERICAL STUDY OF THE URBAN GEOMETRICAL REPRESENTATION IMPACT IN A SURFACE ENERGY BUDGET MODEL

Antonio Cantelli[1], Paolo Monti[1], Giovanni Leuzzi[1]

[1]*Department of Civil and Environmental Engineering, "Sapienza" Università di Roma, Via Eudossiana 18, 00184 Roma, Italy.*

email: paolo.monti@uniroma1.it

Abstract

The aim of this work is to investigate how both the orientation of the urban canyon and the modeling of the edge effects (i.e. urban canyons of finite length) are important in the numerical simulation of the surface energy budget in urban areas. Starting from the Town Energy Balance (TEB) scheme, two models of increasing complexity of the canyon geometry are developed. A sensitivity analysis of the role played by the chosen hypothesis and parameterizations is performed by coupling the canyon schemes with the numerical weather prediction model RAMS. The results suggest that a detailed description of the urban geometry could produce non-negligible differences of the energy balances and of the temperature fields with respect to what occurs using simpler schematizations, in particular during the summer.

Keywords

TEB; Building; Urban Canyon; Urban Heat Island; Energy Balance; Meteorological models

1. Introduction

Air quality, human comfort and energy consumption are good examples on why the modeling of the urban heat island (UHI) is becoming increasingly important. For instance, knowledge of the detailed pattern of the flow field within urban areas is of primary interest for estimations of pollutant dispersion in large cities [1-3]. However, the understanding of the energetic balances and definition of the surface characteristics in a wide range of scales, from the street scale to the city-wide scale [4], are only two of the main problems associated with the UHI analysis.

Numerical weather prediction (NWP) models are a very useful tool to forecast the spatial-temporal evolution of UHIs by means of the integration of the balance equations of mass, momentum, heat and moisture. In the past, the urban area was schematized in NWP models as a 2D entity, which differs from the surrounding rural area only by the changing of the thermal and radiative properties. Recently, several urban canopy schemes have been developed to improve the surface energy balance in urban areas. These schemes are generally single- or multi-layer [5]. In the former type the coupling between the urban canopy and the first atmospheric level of the NWP model is located above the urban canopy (see [6-10] among others). In contrast, in multi-layer schemes it is located within the urban canopy [11-15]. The single-layer approach is easier in its application and it has been demonstrated to be well-suited to analyze the surface energy balance [16,17]. Furthermore, single-layer schemes show a lower bias of the simulated nighttime temperature with respect to the multi-layer approach [18].

The town energy balance (TEB, [6]) is one of the single-layer schemes used by the scientific community. Previous work showed the capability of TEB coupled with NWP models in reproducing the surface energy balance in large cities [19-25]. The TEB has been employed in this paper to investigate the role played by the geometrical approximations adopted in an urban canyon (UC) scheme. The TEB simulates very efficiently the surface energy balance by using a simplified description of the urban geometry. In particular, according to [19], the surface energy balance can be written as:

$$Q^{*} + Q_F = Q_H + Q_E + G^{*} + \Delta Q_A \quad [\mathrm{W\ m^{-2}}] \qquad (1)$$

where Q^* is the net all wave radiation, Q_F the anthropogenic heat flux, Q_H the turbulent sensible heat flux, Q_E the turbulent latent heat flux, G^* the canopy storage heat flux and ΔQ_A the net horizontal advective heat flux. For the sake of simplicity, in this paper Q_F, Q_E and ΔQ_A are set to zero. Taking into account the expression of Q^* in terms of radiative fluxes, equation (1) reads as:

$$Q^* = S\downarrow - S\uparrow + L\downarrow - L\uparrow = Q_H + G^* \qquad (2)$$

Here $L\uparrow$ and $L\downarrow$ are, respectively the outgoing and incoming infrared radiations, while $S\uparrow$ and $S\downarrow$ are the outgoing and incoming solar radiations (Fig. 1), the latter calculated as $S\downarrow = S_{dir} + S_{dif}$, where S_{dir} and S_{dif} represent the solar direct and diffuse radiations.

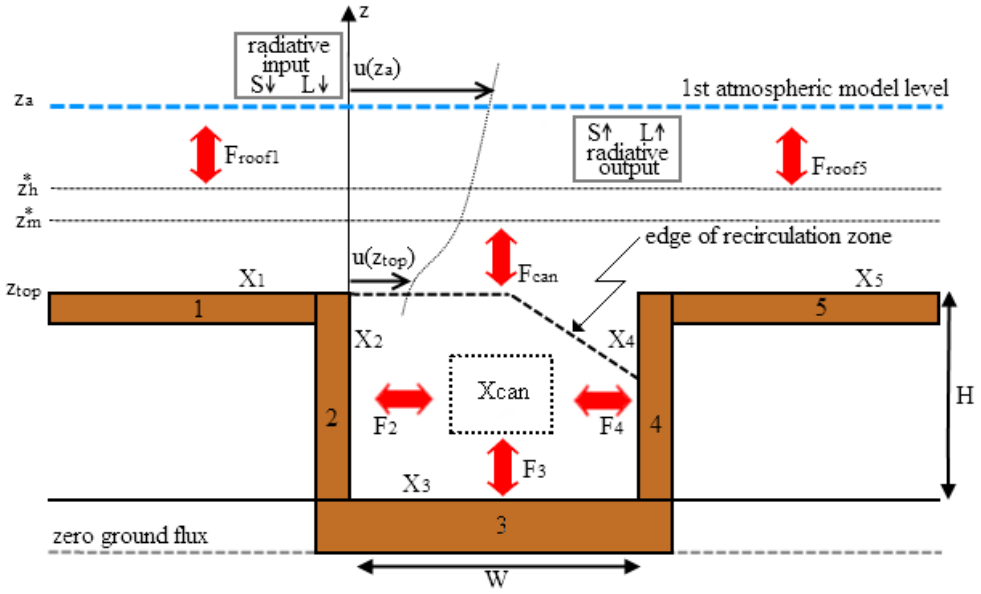

Fig. 1 Sketch of the physical process occurring in an urban canyon of height H and width W. The UC surface consists of two roofs, one road and two walls (numbered hereinafter as to 1, 5, 3, 2 and 4, respectively). Each surface has its own scalar X value (temperature and umidity). The dashed sloped line inside the UC depicts the edge of the recirculation region which form within the UC. $u(z_a)$ is the wind at the first level (z_a) of the NWP model, while $u(z_{top})$ is the wind value at the canyon top. F_{roof} and F_{can} indicate the turbulent fluxes associated, respectively, to the roof and the canyon, the latter composed of the contribution associated to the walls (F_2 and F_4) and the road (F_3).

Since TEB is thought to be coupled with an NWP model, it describes the urban features contained in each grid-cell (of a dimension of a few hundred meters). Three basic hypotheses for the UCs are adopted by the TEB: (i) they are equal among

themselves, (ii) they have infinite length and (iii) they have no preferred orientation. Such an approach implies a spatial mean of the geometrical characteristics of the portion of the urban area contained in each grid-cell and, therefore, of their effects on the turbulent fluxes exchanged by the TEB with the overlaying atmosphere. In accordance with [26], the TEB can be defined as a three-facet scheme since it models the energy budget of the UC by considering the rooftop, the road and one wall, the latter considered as the vertical surface which has a temperature close to the average value between the temperatures assumed by the two facing walls constituting the real UC. Moreover, the infrared radiation is calculated by assuming the UC as a feature of infinite length, i.e., the edge effects are neglected and the UC behaves as a simpler 2D object. Of course, these conditions change the energy budget. On the other hand, the adoption of an average UC orientation plays a fundamental role in the wind speed pattern within the UC as the effects of wind canalization are therefore not modeled explicitly. Such an approximation impedes the knowledge of the actual wind speed within the UC and limits the applicability in urban areas of pollutant dispersion models capable to calculate the concentration field within every single UC (see among others [27,28]).

The TEB scheme is taken here as a zero-level model, hereinafter referred to as L0, consisting in the starting point of successive improvements introduced into the scheme by removing the simplifications cited above. In this way, a sensitivity analysis on the importance of the various simplifications is performed. In particular, the UC scheme accounting for the actual orientation (i.e. a four-facet model, where both the UC walls are modeled) will be hereinafter referred to as L1, while if the hypothesis of infinite length is also removed, a level 2 (L2) model is considered. The three UC schemes, sketched in Fig. 2a, will be coupled with an NWP model in order to compare the role played by the chosen parameters for an idealized but realistic configuration.

The paper is organized as follows. In Sections 2 and 3 the characteristics of the new schemes L1 and L2, respectively, will be described. The numerical setup and details regarding the coupling with the NWP model are reported in Section 4. Section 5 is devoted to the discussion of the results, while conclusions are given in Section 6.

2. Canyon scheme L1

As stated above, L1 is a four-facet model obtained by removing the simplifications related to the adoption of a mean orientation of the UC axis. Therefore, the direction of the UC is accounted explicitly and the different shading of the two walls can be taken into account. This changes the original TEB equations, with regard to the balance of both the solar and infrared energy fluxes (see next subsection). It is also necessary to introduce new laws valid for the turbulent fluxes in order to take into account the effects of wind channeling in the UC as a function of its orientation (see sections 2.2 and 2.3). The new equations are not easy to obtain and only their final expressions are given here. A complete description of the model equations can be found in Cantelli [29]. Moreover, to furnish all the needed information to better understand the study, derivation of the main formulas are provided in a Supplementary Electronic Material.

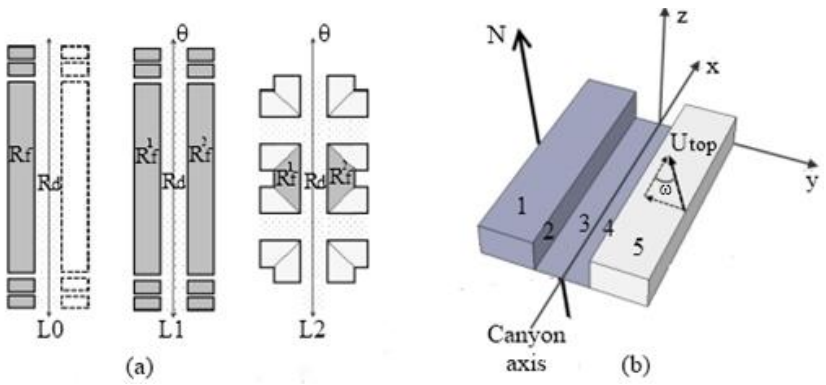

Fig. 2 UC schemes. (a) Infinite UC with average orientation (L0, left), infinite UC with actual orientation θ (L1, center), UC with actual orientation and finite length (right, L2). R_f indicates the roof for L0, while R_f^1 and R_f^2 the roofs for L1 and L2. R_d is the road. (b) The adopted reference system. The numbers indicate the various UC surfaces: 1 the roof with y<0, 2 the wall with y<0, 3 the road, 4 the wall with y>0, 5 the roof with y>0 (y=0 is the UC axis). U_{top} is the wind velocity above the UC while ω is the angle between U_{top} and the canyon axis.

2.1 Short and infrared radiation

The expressions of the direct solar radiation incident on the roofs $S_{1\text{-dir}}=S_{5\text{-dir}}=S_{dir}$ remain unaltered with respect to those for L0 [6] (the surfaces of the UC are numbered as depicted in Figs. 1 and 2b). In contrast, the contributions $S_{2,4-\mathrm{dir}}(\theta)$ and $S_{3-\mathrm{dir}}(\theta)$

referred to the walls and the road, respectively, must be modified (θ is the azimuthal angle between the canyon axis and the North, Fig. 2b). From simple geometrical considerations, it can be shown that:

$$S_{2,4-dir}(\theta) = \begin{cases} sc_{2,4} S_{dir} \tan\lambda |\sin\theta|, & \lambda < \lambda_0 \\ sc_{2,4}\, S_{dir} \frac{W}{H}, & \lambda \geq \lambda_0 \end{cases}, sc_{2,4} = \begin{cases} sc_2 = 0,\ sc_4 = 1,\ \sin\theta < 0 \\ sc_2 = 1,\ sc_4 = 0,\ \sin\theta \geq 0 \end{cases} \quad (3)$$

$$S_{3-dir}(\theta) = \begin{cases} S_{dir}\left(1 - \frac{H}{W}|\sin\theta|\tan\lambda\right), & \lambda < \lambda_0 \\ 0, & \lambda \geq \lambda_0 \end{cases} \quad (4)$$

where H and W are the height and the width of the UC, λ and $\lambda_0 = \text{atan}(H/W)$ are the zenith angle and the zenith critical angle, respectively (see [6] for details). $sc_{2,4}$ is the shading coefficient, that takes into account the alternate lighting of the walls. The presence of both walls implies the addition of new terms in the equations which account for the multiple reflections of the direct incident solar radiation. As for L0, this balance is calculated by considering infinite reflections. In particular, it can be shown that the solar radiations S_i^* absorbed by the surfaces i=2,3,4 are:

$$S_2^* = (1-\alpha_2)(S_{2-dir} + S_{2-dif}) + (1-\alpha_2)(1-2\psi_2)M_4 + (1-\alpha_2)(\psi_2)M_3 \quad (5)$$

$$S_3^* = (1-\alpha_3)(S_{3-dir} + S_{3-dif}) + (1-\alpha_3)(1-\psi_3)(M_2 + M_4)0.5 \quad (6)$$

$$S_4^* = (1-\alpha_4)(S_{4-dir} + S_{4-dif}) + (1-\alpha_4)(1-2\psi_4)M_2 + (1-\alpha_4)(\psi_4)M_3 \quad (7)$$

where α_i, $S_{i,dir}$, S_{i-dif} and ψ_i indicate, respectively, the albedo, the received direct solar radiation, the received diffuse solar radiation and the sky view factor of the i-th surface (i.e. the portion of the sky seen by the i-th surface). The terms multiplied by the factors M_2, M_3 and M_4 (see Appendix A for their definition) on the right hand side of Eqs. (5-7) take into account the effect of the multiple reflections due to the road and the two walls. The solar radiations S_1^* and S_5^* absorbed by the roofs remain unaltered with respect to L0:

$$S_{1,5}^* = \left(1-\alpha_{1,5}\right)\left(S_{1,5-dir} + S_{1,5-dif}\right) \quad (8)$$

With regard to the net infared radiations of the road L_3^* and the two walls L_2^* and L_4^*, it can be shown that (see Supplementary Online Resource):

$$L_2^* = \psi_2\varepsilon_2\varepsilon_3\sigma T_3^4 + (1-2\psi_2)\varepsilon_2\varepsilon_4\sigma T_4^4 + \psi_2\varepsilon_2 L\downarrow - \varepsilon_2\sigma T_2^4 + \varepsilon_2\sigma\psi_2(1-\varepsilon_3)(1-\psi_3)\frac{1}{2}(\varepsilon_2 T_2^4 + \varepsilon_4 T_4^4) + \varepsilon_2\sigma(1-2\psi_2)(1-\varepsilon_4)[(1-2\psi_4)\varepsilon_2 T_2^4 + \psi_4\varepsilon_3 T_3^4] + \varepsilon_2 L\downarrow[\psi_3\psi_2(1-\varepsilon_3) + \psi_4(1-2\psi_2)(1-\varepsilon_4)] \quad (9)$$

$$L_3^* = (1-\psi_3)\varepsilon_3\sigma\frac{1}{2}[\varepsilon_4 T_4^4 + \varepsilon_2 T_2^4] + \psi_3\varepsilon_3 L\downarrow - \varepsilon_3\sigma T_3^4 + \varepsilon_3\sigma(1-\varepsilon_2)(1-\psi_3)\frac{1}{2}[\psi_2\varepsilon_3 T_3^4 + (0.5-\psi_2)\varepsilon_4 T_4^4] + \varepsilon_3\sigma(1-\varepsilon_4)(1-\psi_3)\frac{1}{2}[\psi_4\varepsilon_3 T_3^4 + (0.5-\psi_4)\varepsilon_2 T_2^4] + (1-\psi_3)\varepsilon_3 L\downarrow\frac{1}{2}[\psi_2(1-\varepsilon_2) + \psi_4(1-\varepsilon_4)] \quad (10)$$

$$L_4^* = \psi_4\varepsilon_4\varepsilon_3\sigma T_3^4 + (1-2\psi_4)\varepsilon_2\varepsilon_4\sigma T_2^4 + \psi_4\varepsilon_4 L\downarrow - \varepsilon_4\sigma T_4^4 + \varepsilon_4\sigma\psi_4(1-\varepsilon_3)(1-\psi_3)\frac{1}{2}(\varepsilon_2 T_2^4 + \varepsilon_4 T_4^4) + \varepsilon_4\sigma(1-2\psi_4)(1-\varepsilon_2)[(1-2\psi_2)\varepsilon_4 T_4^4 + \psi_2\varepsilon_3 T_3^4] + \varepsilon_4 L\downarrow[\psi_3\psi_4(1-\varepsilon_3) + \psi_2(1-2\psi_4)(1-\varepsilon_2)] \quad (11)$$

where σ is the Stefan-Boltzmann constant. ϵ_i and T_i indicate, respectively, the infrared emissivity and the temperature of the i-th surface. The net infrared radiations L_1^* and L_5^* of the roofs coincide with those of L0 [6].

2.2 Flow and turbulence in the roughness sublayer

One of the problems encountered in modeling the UHI is the definition of suitable laws for the vertical profiles of the wind velocity, temperature and humidity in the roughness sublayer (RS), i.e. the layer between the surface and the inertial layer (IL), where the flow adjusts to the effects of the buildings and the turbulent fluxes are not constant with height [30]. As is well known, the Monin-Obukhov similarity theory does not apply in the RS, in that the Reynolds stress is not a constant therein but grows in proximity to the transition between IL and RS (see for example [31]). To take into account this behaviour, [31,32] analysed the dependence of the friction velocity u_* on z. In particular, for neutral conditions we use the semi-empirical law derived by [32] for the vertical profile of the mean wind speed $u_{RS}(z)$ valid in the RS, viz.,

$$u_{RS}(z) = \frac{u_*}{0.6k}\left[1 - 0.6\ln(0.12) - \exp\left(0.6 - 0.072\frac{z-d_0}{z_0}\right)\right] \quad (12)$$

where k=0.4 is the von Karman constant, $d_0 = \bar{H}0.4\lambda_p\exp[-2.2(\lambda_p-1)] + 0.6\lambda_p$ the displacement height, $z_0 = \bar{H}0.072\lambda_p\{\exp[-2.2(\lambda_p-1)] - 1\}$ the roughness length, $\bar{H}$

the average height of the building while $\lambda_p = A_p/A_T$, where A_P is the average plan area of roughness elements and A_T the total surface area. z_0 and d_0 are derived from the parameters of the regression lines of the vertical profile of the Reynolds stress, while u_* is calculated within the IL at a reference height [32].

A question arises as to the fact that eq. (10) is valid only in the case of neutral atmosphere. The method proposed by [33], found on a previous work of [34], is therefore used to extend the model also to stable and unstable conditions. In particular, based on the classical relationships for the wind speed gradient, [34] proposed:

$$\frac{kz}{u_*}\frac{\partial u}{\partial z} \cong \Phi_m(z/L)\ \varphi_m(z/z_{*m}) \tag{13}$$

$$\frac{kz}{\theta_*}\frac{\partial \theta}{\partial z} \cong \Phi_h(z/L)\ \varphi_h(z/z_{*h}) \tag{14}$$

where $\Phi_m[z/L]$ and $\Phi_h[z/L]$ are the classical universal dimensionless functions [35] that equal 1 when the Obukhov length $L = -u_*^3(\kappa q_0)^{-1} \rightarrow \infty$ (here q_0 is the buoyancy flux). The functions φ_m and φ_h incorporate the effects of the RS. z_{*m} and z_{*h} (Fig. 1) are the heights where $\varphi_m(z/z_{*m})$=1 and $\varphi_h(z/z_{*h}) = 1$, respectively. In order to solve eqs. (13,14), [33] introduced the following expressions:

$$\varphi_m(z/z_{*m}) = 1 - e^{-\mu_m \frac{z}{z_{*m}}} \tag{15}$$

$$\varphi_h(z/z_{*h}) = 1 - e^{-\mu_h \frac{z}{z_{*h}}} \tag{16}$$

where the parameters μ_m and μ_h were determined empirically from data referred to a vegetated canopy [36]. In our case, since it is expected that urban canopies behave differently from vegetated ones, μ_m and μ_h are not known. Thus, in this work $\varphi_m(z/z_{*m})$ is estimated indirectly from the vertical profile $u_{RS}(z)$. This procedure is not reported here and only the results are given (details can be found in [29]). The vertical profile of the wind speed valid in diabatic conditions assumes the form:

$$u(z) = \frac{u_*}{k}[\ln(z/z_0) - \Psi_m(z/L) - \Psi_m(z_0/L) + \Psi_m^*(z/L, z/z_{*m})] \tag{17}$$

where $z_{*m} \cong d_0 + 8.4\, z_0$, while:

$$\Psi_m^*(z/L, z/z_{*m}) = \Phi_m \left[\left(1 + \frac{\nu}{\mu_m \frac{z}{z_{*m}}}\right)\frac{z}{L}\right]\frac{1}{\eta}\left(1 + \frac{\eta}{\mu_m \frac{z}{z_{*m}}}\right)e^{-\mu_m \frac{z}{z_{*m}}} \tag{18}$$

is the integral of $\varphi_m(z/z_{*m})$, $\mu_m \cong 2.4$, $\eta \cong 1.5$ and $\nu \cong 0.5$, The integral Ψ_m of the stability function is solved by using the analytical method of [37]. Similarly, for the potential temperature profile T_p:

$$T_p(z) - T_{p0} = \frac{T_{p*}}{k}[\ln(z/z_{0h}) - \Psi_h(z/L) - \Psi_h(z_{0h}/L) + \Psi_h^*(z/L, z/z_{*h})] \quad (19)$$

where T_{p0} is the potential temperature at $z_{*h} \cong 2.3\overline{H}$, T_{p*} the temperature scale and Ψ_h^* the termodynamic counterpart of Eq. (18) with $\mu_h \cong 0.95$. The vertical profile of the humidity (not reported here) is analogous to that for the temperature.

Finally, the aerodynamic resistances (see next section) referred to the advection of the generic scalar X (temperature and humidity) takes the form [38]:

$$r_X = [C_X u(z)]^{-1} \quad (20)$$

where the drag coefficient in bulk form C_X is [35]:

$$C_X = \frac{\kappa^2}{Pr}[\ln(z/z_0) - \Psi_m(z/L, z_0/L) + \Psi_m^*(z/L, z/z_{*m})]^{-1} \times [\ln(z/z_{0X}) - \Psi_X(z/L, z/z_{0X}) + \Psi_X^*(z/L, z/z_{*X})]^{-1} \quad (21)$$

The Prandtl number Pr has been set equal to 1.

2.3 Flow and turbulence in the urban canyon

The exact determination of both the wind speed, temperature, humidity and turbulent fluxes within the UC is a difficult task, in particular if its orientation is taken into account. The wind velocity parallel to the UC axis we adopt in this work is the one proposed by [39]. These authors, on the basis of numerical simulations, calculated the expression of the wind velocity along the UC axis $u_{//}$ as the spatial average over the area (H·W) perpendicular to the UC:

$$u_{//} = u_{ctp}\frac{\delta_0^2}{HW}\left[\frac{2\sqrt{2}}{C}(1-\beta_*)\left(1-\frac{\pi}{2}H_1(C)\right) + \beta_*\frac{2\alpha_*-3}{\alpha_*} + \left(\frac{W}{\delta_0}-2\right)\frac{\alpha_*-1}{\alpha_*}\right] \quad (22)$$

where:

$$\alpha_* = \ln\left(\frac{\delta_0}{\overline{z_0}}\right) \text{ and } \beta_* = \exp\left[\frac{C}{\sqrt{2}}\left(1-\frac{\delta_0}{\overline{z_0}}\right)\right] \quad (23)$$

U_{top} is the velocity at the UC top derived with Eq. (12) or (17), $u_{ctp}=U_{top}\cos(\omega)$ is its component parallel to the canyon axis, ω is the angle between U_{top} and the canyon axis (Fig. 2b), $\overline{z_0}$ is the average roughness length of the UC surfaces, $\delta_0=\min(H, W/2)$, while C is a parameter depending on z_0, δ_0 and on the Bessel functions. To reduce the CPU time during the numerical simulation, the approximated form of C reported in Appendix B is used. The function $\frac{\pi}{2}H_1(C)$ is calculated for $0 < C \leq 1$ using Eq. (22) reported in [39].

With regard to turbulent fluxes, temperature and humidity, a distintion between the type of flow is necessary as those variables can depend on the aspect ratio H/W [38]. Following [40], three types of flow regime can be recognized as a function of the extension of the recirculation zone (Fig. 1) or as a function of the H/W: the "skimming flow regime" (SFR), the "wake interference flow regime" (WIFR) and the "isolated roughness flow regime" (IRFR). The SFR is typical of narrow UCs where H/W>2/3, the IRFR applies for wide UCs (H/W<1/3), while the WIFR refers to intermediate UCs (1/3<H/W<2/3). Since the sensitivity analysis conducted in this paper regards UCs with H/W=0.5, 1 and 1.5, in what follows only the SFR and WIFR cases are considered.

The turbulent flux $F_s = \overline{u_s' X'}$ of the generic scalar X along the direction s, can be expressed in bulk form as $F_s = \Delta X / r_X$. Here, prime indicates fluctuation around the mean and the bar the operation of time averaging. The total amount of flux F_t referred to the whole UC can be assumed as the sum of the contribution associated to the roofs, F_{roofs} (which is independent of the flow regime), and F_{can}, which incorporates the road and the two walls contribution (see Fig. 1):

$$F_t = \frac{S_{roofs}F_{roofs}+S_{can}F_{can}}{S_{roofs}+S_{can}} \tag{24}$$

where S_{roofs} and S_{can} are the total roof and canyon areas. In bulk form, F_{roofs} is given by [38]:

$$F_{roofs} = \frac{S_{roof-1}}{r_1 S_{roofs}}(X_1 - X_a) + \frac{S_{roof-5}}{r_5 S_{roofs}}(X_5 - X_a) \tag{25}$$

whathever the type of regime. X_1 and X_5 are the values of X at the roofs, while X_a that at the first grid node of the NWP model. r_1 and r_5 are the corresponding aerodynamic resistances (Eq. 20), while S_{roof-1} and S_{roof-5} are the roof 1 and 5 area, respectively, being $S_{roofs} = S_{roof-1} + S_{roof-5}$. Note that the two roofs surfaces, even if they have the

same extension according to L1 representation, are explicitely treated because each of them is influenced by its own internal building temperature, wich is calculated as suggested by [19]. The contribution of the canyon, F_{can}, depends on the type of regime. For the SFR regime one has [38]:

$$F_{can} = \frac{1}{r_{can}}(X_{can} - X_a) \tag{26}$$

where X_{can} is calculated by means of the balance of the turbulent flux exchanged between the UC surfaces and the atmosphere above. It can be shown [29] that:

$$X_{can} = \left[\frac{H}{W}\left(\frac{X_2}{r_2} + \frac{X_4}{r_4}\right) + \frac{X_3}{r_3} + \frac{X_a}{r_{can}}\right] / \left[\frac{H}{W}\left(\frac{1}{r_2} + \frac{1}{r_4}\right) + \frac{1}{r_3} + \frac{1}{r_{can}}\right] \tag{27}$$

Analogous considerations can be made for the WIFR regime, extending Eq. (27) by taking into account the recirculation region (Fig. 1) within the UC [38]. The aerodynamic resistances r_2, r_3, r_4 can be determined by means of the following equation [29]:

$$r_j = \ln\left(\frac{0.1H}{z_{0,j}}\right)\ln\left(\frac{0.1H}{z_{0,X_j}}\right)\left(\kappa^2\sqrt{u_j^2 + u_{//}^2}\right)^{-1} \quad \text{with j=2,3,4} \tag{28}$$

which extends the one reported in [38] by including the effect of the wind velocity along the UC axis $u_{//}$. Note that unlike what is done for the RS, in Eq. (28), the atmospheric stability is not considered for the calculation of the aerodynamic drag within the UC. This is due to the lack of knowledge of both the effects of the stability and the actual distribution of the average speed within the UC. For the aerodynamic resistance r_{can}, calculated between the canyon and the RS, Eqs. (27-28) are used. In accordance with [20], $z_{0,2}$=$z_{0,4}$=0.15 and $z_{0,3}$=0.05 are set within the UC, while for the roofs $z_{0,1}$=$z_{0,5}$=0.15.

The calculation of X_{can} in Eq. (27) implies the determination of the X_j for all the UC surfaces. This was done by solving a prognostic equation that describes the evolution of the scalar X for each surface. Following [6], for temperature one has:

$$\frac{\partial T_j}{\partial t} = \frac{1}{C_j d_j}[S_j^* + L_j^* - F_j - I_j] \tag{29}$$

where S^* and L^* are calculated by Eqs. (5-11), C_j and d_j are respectively the thermal capacity [M $Jm^{-3}K^{-1}$] and the thickness [m] of the j-th surface, I_j is the conduction heat flux exchanged with the underlying wall layers, F_j is the sensible heat flux exchanged by

the j-th surface (see Fig. 1) with the canyon air (for j=2,3,4) or with the first atmospheric model layer (for j=1,5). For the surfaces j=2,3,4, the turbulent heat flux $F_j = r_j^{-1}(T_j - T_{can})$ is solved in a similar way to Eq. (26) once the r_j is calculated according to Eq. (28). For the other scalarar quantities, expressions similar to Eq. (29) are used.

3. Canyon scheme L2

L2 differs from L1 in that the hypothesis of UCs of infinite length is also removed. The UC edges present a crossroad from which other canyons originate. To simplify the analysis, UCs are assumed perpendicular among themselves (Fig. 3a), with the same length and aspect ratio. The energy balances of the elements costituing the L2 scheme, i.e. the "main" UC, 6 "secondary" UCs and 2 crossroads (the plane areas limiting the main UC), are calculated separately. Crossroads are limited by vertical surfaces of little extension with respect to that of the UC walls. To identify the different surfaces considered in the scheme, the nomenclature introduced in the previous section is extended. In particular, subscript "cr" indicates crossroads.

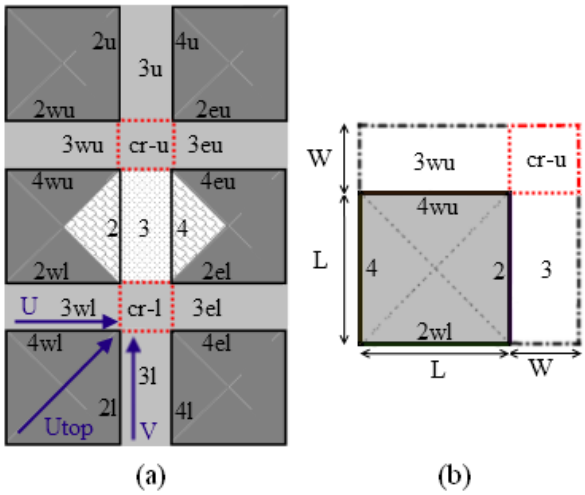

Fig. 3 (a) Planar view of the horizontal surfaces considered in L2. The road and roofs of the main UC are in light grey. 2 and 4 indicate the walls while 3 the road. w, e, u, l, cr indicate, respectively, west, east, upper, lower and crossroad surfaces (in red). The arrow is the wind speed U_{top} at the UC top, U and V are the canyon averaged velocity components flowing within two perpendicular UCs calculated by using Eq. (22). (b) The simplified version of L2.

To distinguish the main UC from the other canyons, subscripts “u” and “l” indicate upper and lower location of the secondary UCs with respect to the main UC, respectively, while “e” and “w” refer to east and west locations. To differentiate the secondary UCs positions with respect to the upper and lower sides, subscripts u and l are used in combination with e and w. In this way, subscript 2u indicates the surface located in the upper side of the main UC, while 3el the road referred to the UC located in the lower east side (Fig. 3a). As in the case of L1, L2 requires the definition of new equations describing solar and infrared radiations.

3.1. Solar and infrared radiations

Shadowing in L2 does not differ from that modeled in L1 (Eqs. 5 and 6). In contrast, the finite length of the UC implies the definition of new relations for the view factors. With regard to the main UC, the view factors of the wall facing the road and that of the opposite surface are, respectively [41,42]:

$$\psi_{3,i} = \frac{1}{2\pi}\int_A \{(\gamma_2 - \gamma_1) + \cos\beta[\tan^{-1}(\cos\beta\tan\gamma_1) - \tan^{-1}(\cos\beta\tan\gamma_2)]\}\,dA \qquad (30)$$

$$\psi_{i,j} = \frac{1}{2\pi}\int_A \begin{bmatrix}\sin\gamma_2\tan^{-1}(\tan\delta_2\sin\gamma_2) + \sin\beta\tan^{-1}(\cot\delta_2\sin\beta) + \\ +\sin\gamma_1\tan^{-1}(\tan\delta_1\sin\gamma_1) + \sin\beta\tan^{-1}(\cot\delta_1\sin\beta)\end{bmatrix} dA \qquad (31)$$

where i,j=2,4 with i≠j. The angles γ_1, γ_2, β, δ_1 and δ_2 are shown in Fig. 4.

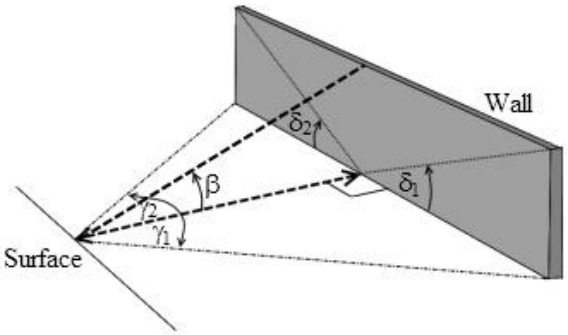

Fig. 4 Schematization of the radiative exchanges by a surface element and a wall of finite length. The angles β, δ_1 and δ_2 are positive along the vertical plane, while $\gamma_1>0$ and $\gamma_2<0$ belong to the horizontal plane (adapted from [41]).

In both the integrals, A is the road and the wall surfaces for $\psi_{3,i}$ and $\psi_{i,j}$, respectively. The view factor with two indices differs from that with one index: $\psi_{i,j}$ indicates the portion of the j-th surface seen by the i-th surface. Note that in the presence of the sole main UC, the sky view factor of the street is $\psi_3=(1-2\psi_{3,i})$, while that of the wall is $\psi_2=(0.5-\psi_{i,j})$ [6]. When the other UCs are present, from simple geometrical considerations it can be shown that the sky view factors of the surfaces of the main UC are:

$$\begin{cases} \psi_2 = \psi_{2,3} + 2(\psi_{2,\mathrm{cr}} + \psi_{2,3\mathrm{eu}\infty} + \psi_{2,3\mathrm{u}\infty}) \\ \psi_3 = 1 - \left(2\psi_{3,2} + 4\psi_{3,2\mathrm{u}\infty} + 4\psi_{3,2\mathrm{eu}\infty}\right) \\ \psi_4 = \psi_{4,3} + 2(\psi_{4,\mathrm{cr}} + \psi_{4,3\mathrm{eu}\infty} + \psi_{4,3\mathrm{u}\infty}) \end{cases} \quad (32)$$

where ∞ indicates that the surfaces located beyond the crossroads have, in the radiation calculation phase, infinite length (i.e., the effects of subsequent crossroads are neglected for simplicity). Once the view factors of the surfaces are calculated, the net infrared radiation for the streets and the walls of the main UC can be determined. In particular, it can be shown that (see Supplementary Online Resource):

$$\mathrm{L}_2^* = \psi_{3,2}\varepsilon_2\varepsilon_3\sigma\mathrm{T}_3^4 + 2\psi_{2,4}\varepsilon_2\varepsilon_4\sigma\mathrm{T}_4^4 + \psi_2\varepsilon_2\mathrm{L}\downarrow$$
$$-\varepsilon_2\sigma\mathrm{T}_2^4 + \varepsilon_2\sigma\psi_{3,2}(1-\varepsilon_3)2\psi_{3,2}\frac{1}{2}(\varepsilon_2\mathrm{T}_2^4 + \varepsilon_4\mathrm{T}_4^4) + \varepsilon_2\sigma 2\psi_{2,4}(1-\varepsilon_4)\left[2\psi_{4,2}\varepsilon_2\mathrm{T}_2^4 + \right.$$
$$\left.\psi_{4,3}\varepsilon_3\mathrm{T}_3^4\right] + \varepsilon_2\mathrm{L}\downarrow\left[\psi_3\psi_{2,3}(1-\varepsilon_3) + \psi_4 2\psi_{2,4}(1-\varepsilon_4)\right] + \mathrm{L}_2^{\mathrm{ed}} \quad (33)$$

$$\mathrm{L}_3^* = \psi_{3,2}\varepsilon_3\sigma[\varepsilon_4\mathrm{T}_4^4 + \varepsilon_2\mathrm{T}_2^4] + \psi_3\varepsilon_3\mathrm{L}\downarrow - \varepsilon_3\sigma\mathrm{T}_3^4 + \varepsilon_3\sigma(1-\varepsilon_2)2\psi_{3,2}\frac{1}{2}\left[\psi_{3,2}\varepsilon_3\mathrm{T}_3^4 + \right.$$
$$\left.\psi_{2,4}\varepsilon_4\mathrm{T}_4^4\right] + \varepsilon_3\sigma(1-\varepsilon_4)2\psi_{3,2}\frac{1}{2}\left[\psi_{4,3}\varepsilon_3\mathrm{T}_3^4 + \psi_{4,2}\varepsilon_2\mathrm{T}_2^4\right] + 2\psi_{3,2}\varepsilon_3\mathrm{L}\downarrow\frac{1}{2}[\psi_2(1-\varepsilon_2) +$$
$$\psi_4(1-\varepsilon_4)] + \mathrm{L}_3^{\mathrm{ed}} \quad (34)$$

$$\mathrm{L}_4^* = \psi_{4,3}\varepsilon_4\varepsilon_3\sigma\mathrm{T}_3^4 + 2\psi_{4,2}\varepsilon_2\varepsilon_4\sigma\mathrm{T}_2^4 + \psi_4\varepsilon_4\mathrm{L}\downarrow$$
$$-\varepsilon_4\sigma\mathrm{T}_4^4 + \varepsilon_4\sigma\psi_{4,3}(1-\varepsilon_3)2\psi_{3,2}\frac{1}{2}(\varepsilon_2\mathrm{T}_2^4 + \varepsilon_4\mathrm{T}_4^4) + \varepsilon_4\sigma 2\psi_{4,2}(1-\varepsilon_2)\left[2\psi_{2,4}\varepsilon_4\mathrm{T}_4^4 + \right.$$
$$\left.\psi_{2,3}\varepsilon_3\mathrm{T}_3^4\right] + \varepsilon_4\mathrm{L}\downarrow\left[\psi_3\psi_{4,3}(1-\varepsilon_3) + \psi_2 2\psi_{4,2}(1-\varepsilon_2)\right] + \mathrm{L}_4^{\mathrm{ed}} \quad (35)$$

where $\mathrm{L}_2^{\mathrm{ed}}$, $\mathrm{L}_3^{\mathrm{ed}}$ and $\mathrm{L}_4^{\mathrm{ed}}$ are related to the infrared radiation coming beyond the edges of UC (superscript "ed") from the surfaces located beyond the crossroads:

$$L_2^{ed} = \varepsilon_2\varepsilon_w\psi_{2,4u}\sigma(T_{4u}^4 + T_{4l}^4) + \varepsilon_2\varepsilon_w\psi_{2,2eu}\sigma(T_{2eu}^4 + T_{4el}^4) + \varepsilon_2\varepsilon_3\sigma\left[\psi_{2,3u}(T_{3u}^4 + T_{3l}^4) + \right.$$
$$\left. + \psi_{2,cr-u}(T_{cr-u}^4 + T_{cr-l}^4) + \psi_{2,3eu}(T_{3eu}^4 + T_{3el}^4)\right] \quad (36)$$

$$L_3^{ed} = \varepsilon_3\varepsilon_w\psi_{3,2u}\sigma(T_{4u}^4 + T_{2u}^4 + T_{4l}^4 + T_{2l}^4) +$$
$$+\varepsilon_3\varepsilon_w\psi_{3,2eu}\sigma(T_{2eu}^4 + T_{4el}^4 + T_{4wl}^4 + T_{2wu}^4) \quad (37)$$

$$L_4^{ed} = \varepsilon_4\varepsilon_w\psi_{4,2u}\sigma(T_{2u}^4 + T_{2l}^4) + \varepsilon_4\varepsilon_w\psi_{4,2wu}\sigma(T_{2wu}^4 + T_{4wl}^4) + \varepsilon_4\varepsilon_3\sigma\left[\psi_{4,3u}(T_{3u}^4 + T_{3l}^4) + \right.$$
$$\left. \psi_{4,cr-u}(T_{cr-u}^4 + T_{cr-l}^4) + \psi_{4,3wu}(T_{3wu}^4 + T_{3wl}^4)\right] \quad (38)$$

The last three equations are written considering the geometrical simplification previously adopted for the L2 representation. In essence, that produces the following identity among edge surface-view factors: $\psi_{i,ju} = \psi_{i,jl}$, $\psi_{i,jeu} = \psi_{i,jel}$, $\psi_{i,jwu} = \psi_{i,jwl}$. For the sake of simplicity, it is also assumed that all the walls surfaces located beyond the edges have the same emissivity, ε_w. For practical application, due to the little magnitude of the edge surface-view factors in the edge effects calculation, the temperature differences among the faced walls located beyond the edges could be neglected. For this reason it could be assumed that $L_4^{ed} = L_2^{ed}$.

The equation system (33-38) allows the net infrared radiation for all the main UC surfaces to be evaluated. With regard to the turbulent fluxes, the same relationships defined for L1 are used.

3.2 - Crossroads

3.2.1 Solar radiation at the crossroads

By using the same approach described for L1, the solar radiation is calculated from a simple geometrical analysis, from which an explicit estimation of the area illuminated by the sun is obtained. Once the two shadowing factors $sf(\theta_i)$ related to the two canyons perpendicular between them are calculated [29]:

$$sf(\theta_i) = \begin{cases} 1 - \left(\frac{S_{3-dir}(\theta_i)}{S_{dir}}\right), & S_{dir} > 0 \\ 1, & S_{dir} = 0 \end{cases} \quad (39)$$

one obtains:

$$S_{dir-cr} = S_{dir}\left[1 - sf(\theta_i)\, sf(\theta_j)\right] \quad (40)$$

where the indexes $i \neq j$ indicate the contributions of two distinct UCs mutually perpendicular, which originate in the crossroad.

3.2.2 Infrared radiation at the crossroads

At the crossroads, the infrared radiation balance is described employing the same approach used for the main UC in which the net infrared radiation term is calculated from the incoming and outgoing infrared radiation terms. Therefore, the net infrared radiation for the crossroads reads as:

$$L^{*}_{3cr-i} = \left(1 - 8\psi^{\infty}_{cr-i,2}\right)\varepsilon_3 L\downarrow - \varepsilon_3\sigma T^4_{cr-i} + L_3^{cr-i} \quad (41)$$

where the index i=u,l indicates the upper or lower crosses. $\psi^{\infty}_{cr-i,2}$ is the wall view factor of the crossroad assuming UCs of infinite length, T_{cr-i} is the crossroads surface temperature and L_3^{cr-i} which describes the contribution of the surfaces facing the crossroads, read as (see Supplementary Online Resource):

$$L_3^{cr-i} = \psi_{cr-i,2}\varepsilon_w\varepsilon_3\sigma(T_2^4 + T_{2ei}^4 + T_{2wi}^4 + T_{2i}^4 + T_4^4 + T_{4ei}^4 + T_{4wi}^4 + T_{4i}^4) + \psi_{4,2}\psi_{cr-i,2}(1 - \varepsilon_w)\varepsilon_3\sigma(T_2^4 + T_{2ei}^4 + T_{2wi}^4 + T_{2i}^4 + T_4^4 + T_{4ei}^4 + T_{4wi}^4 + T_{4i}^4) \quad (42)$$

Note also that the terms related to the reflections among the surfaces are neglected in Eq. (41). This simplification is not relevant; in fact, as $\psi_{cr\text{-}i,2} << \psi_{2,3}$ and $\psi_{cr\text{-}i,2} << \psi_{2,4}$, the contribution of the reflections associated to the products of the view factors is small if compared to the other terms of Eq. (41).

3.2.3. Wind velocity and turbulent fluxes at the crossroads

The bulk approach adopted for L1 is used also for L2. Equation (24) is assumed to be a good estimate of the turbulent flux of the generic scalar X exchanged between the UC and the overlying atmosphere. However, an additional complication derives from the advection of scalars from the UCs converging in the air volume above the crossroad. Such a term can be estimated starting from the balance equation of the generic scalar. Neglecting the contributions associated to non-stationarity, to the transport along the z-axis and to the turbulent fluxes along x- and y-axis, one has:

$$\frac{\partial \overline{w'X'}}{\partial z} = -\left(U\frac{\partial X}{\partial x} + V\frac{\partial X}{\partial y}\right) \quad (43)$$

where w' is the vertical velocity fluctuation, while U and V are the velocities parallel to the canyons which converge in the crossroad (see Fig. 3a) obtained from Eq. (22). Adopting the bulk formulation of the turbulent fluxes, Eq. (43) in dicretized form is [29]:

$$X_{can}^{cr} = \left[\frac{X_{cr}}{r_{cr}} + \frac{X_a}{r_{can}} + \frac{H}{W}\left(U\Delta X_i + V\Delta X_j\right)\right] / \left[\frac{1}{r_{cr}} + \frac{1}{r_{can}}\right] \quad (44)$$

where r_{cr} is the resistance to the transport for the crossroad surface calculated from Eq. (28), and where $i \neq j$ as in Eq. (40) indicate the contributions of two distinct UCs mutually perpendicular, which originate in the crossroad. Analogously to the crossroad, the extension of Eq. (27) which includes the contribution of the advection is [29]:

$$X_{can} = \left[\frac{H}{W}\left(\frac{X_2}{r_2} + \frac{X_4}{r_4}\right) + \frac{X_3}{r_3} + \frac{X_a}{r_{can}} + \frac{u_{//}H}{L}\Delta X\right] / \left[\frac{H}{W}\left(\frac{1}{r_2} + \frac{1}{r_4}\right) + \frac{1}{r_3} + \frac{1}{r_{can}}\right] \quad (45)$$

At the crossroads, the use of Eq. (44) requires information on X_{cr}. Its determination, according to Eq. (28), requires the knowledge of the horizontal wind speeds in the vicinity of the surfaces. To simplify the formulation we assume the wind speeds as the average between the mean velocities U and V referred to the two perpendicular canyons (Fig. 3a).

3.3. Coupling of L2 in a NWP model

As is shown above, L2 calculates at each time step the temperatures of the surfaces included in the energetic balance (see Eqs. 33-38 and 41-42). To simplify the model and decrease the CPU time, a simplified procedure that reduces the number of the resolved canyons (in a bulk sense) is adopted. The application of L2, in fact, is based on the solution of the energetic budgets for the main UC, for the two crossroads and for the 6 secondary UCs. Considering that 5 prognostic equations are needed for each UC (as in L1), other 6x5=30 prognostic equations for the 6 canyons and 4 equations for the crossroads are involved. However, the procedure can be simplified by assuming that the geometrical configuration depicted in Fig. 3a is extended to a horizontal surface of infinite area and that the UCs have the same H/W, length, thermal properties and geometry. In doing so, the temperatures of surfaces 2, 3 and 4 coincide with those of

surfaces 2u, 3u, 4u and 2l, 3l and 4l. Similarly, the temperatures of surfaces 2wu, 3wu and 4wu are equal to those of 2eu, 3eu and 4eu. Since this configuration is the same in the whole computational domain, the temperatures 2wu, 3wu and 4wu are equal to 2wl, 3wl, 4wl and 2el, 3el, 4el. For the same reason the two crossroads share the same temperature. With this in mind, the geometrical configuration of L2 passes from 7 canyons and two crossroads to a much simpler one with only 2 canyons perpendicular between themselves and 1 crossroad. The geometrical properties needed to represent L2 (length of the two canyons and aspect ratio) are contained in the characteristics of one of the buildings constituting the canyon array, in the areal extensions of the two roads and in one crossroad (Fig. 3b). This approach significantly simplifies Eqs. (36-38) and (42) as reported in the Supplementary Online Resource. One of the aspects that makes this approach very useful is that it is easy to link with digital terrain models for urban areas because the spatial recognition of the blocks is much simpler with respect to the case of a geometry based on the single UC.

4. Numerical Setup

The three UC schemes described above have been integrated in to the model RAMS 6.0 by a two–way connection. RAMS [43] is a non-hydrostatic, prognostic model able to predict the evolution of the atmosphere through the integration in space and time of the balance equations of mass, momentum, heat, moisture and turbulent kinetic energy. To describe the surface energy balance, RAMS adopts the LEAF3 (Land Ecosystem-Atmospheric Feedback) scheme [44], which is based on biophysical parameters such as the roughness length, displacement height, albedo, emissivity, fractional coverage and leaf area index. However, LEAF3 works well for rural environments, but does not seem to be suitable for urban area applications [23].

The core of the integrated system consists of an interface between RAMS and the canyon scheme. Such interface recognises the ‘rural’ or ‘urban’ nature of each surface node of the numerical grid; if the node is ‘rural’, the surface energy budget is computed by the LEAF3 routine integrated in the original RAMS, otherwise (i.e. for ‘urban nodes’) the canyon model is activated. In the latter case, the interface assigns to the urban node the contribution of all the urban canyons which are contained within the domain of

influence of the node. Thus, starting from the geometrical and physical characteristics of each canyon, the integrated system solves the energy budget corresponding to the considered surface grid node. In particular, for each time step, sensible heat flux, latent heat flux and infrared radiation will be computed as well as the corresponding values of mass, energy humidity and momentum fluxes exchanged between the urban canopy and the first 'air node' above it belonging to the numerical grid of RAMS.

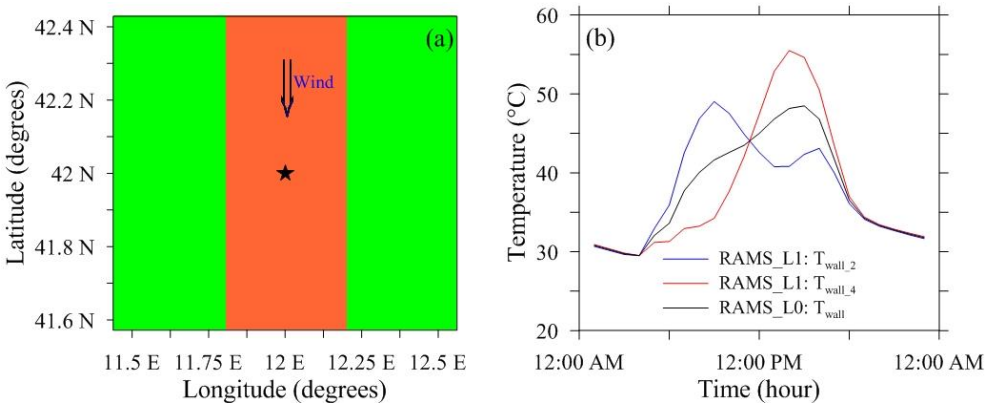

Fig. 5 (a) The domain of the numerical experiments. Colors represent the landuse (green: Mediterranean shrubs; orange: urban area), the blue arrow indicates the wind direction while the black star the location of the vertical profiles used for the analysis. (b) Daily variation of walls temperature [°C] calculated by RAMS-L1 (red and blue lines) for θ=45°, and by RAMS-L0 (black line) for aspect ratio H/W=0.5.

Three integrated systems are used, i.e. RAMS-L0, RAMS-L1 and RAMS-L2, and several numerical experiments have been performed to quantify the differences among the UC schemes. To simplify the sensitivity analysis and to isolate the role played by the geometrical representation in the energy fluxes calculation, a computational domain with simple topography and land use is considered (Fig. 5a). The domain is flat, with planar area of 96×96 km^2. The horizontal grid spacing is 1 km. 44 levels extend vertically up to about 21000 m above sea level; the first node on the vertical line is placed at an altitude of 10 m above ground level over rural terrain and above roof level over urban terrrain. The chosen land use presents three strips of terrain as shown in Fig. 5a. Two of them, each about 31 km wide, located at the edges of the domain, are covered with Mediterranean shrubs; the central strip is a 33 km wide piece of urban land. Each run starts at 06 LST (local standard time), has a duration of 48 hours and is carried out in two

distinct weather conditions to test the response of the UC model to different initial conditions and boundary forcings.

The first group of runs is conducted in typical summer conditions, which correspond, with regard to the insolation level, to the values observed from June 20 to 23 at a latitude of 42 °N. The second group of runs is conducted for the winter season (December 21-24). The simulations are initialized with wind, temperature and humidity vertical profiles taken from radio soundings collected at the Pratica di Mare Airport (LIRA), near Rome (Italy). The vertical profiles are derived interpolating the averages taken during persistent wind conditions. With regard to the wind direction, an almost vertically constant profile is chosen, with the prevailing direction parallel to the urban strip for the whole height of the plabetary boundary layer (arrow in Fig. 5a). This procedure is adopted to limit advection above the urban nodes of sensible and latent heat fluxes coming from surrounding rural areas, hence making it possible to consider $\Delta Q_A=0$ in Eq. (1).

Three simulations are conducted with RAMS-L0 for H/W=0.5, 1 and 1.5, while for RAMS-L1 and RAMS-L2 four runs for each aspect ratio are performed by varying the canyon orientation. In particular, angles of 0°, 45°, 90° and 135° measured clockwise from North are considered for the analysis. The building height is the same for all the cases (H=20 m) and so is the plan areal fraction ($\lambda_p=0.5$). The chosen λ_p value (0.5), appears as a more suitable value for the southern european and mediterranean cities [4].

The comparability of the results obtained with the three UC schemes implies that the condition that all UCs have the same λ_p is attained. Since L2 has two mutually orthogonal UCs and one crossroad between them, it can be shown (Appendix C) that λ_p is maintained (assuming that the two UCs have the same length, H and H/W) if the UC length L is:

$$L = W\left(-1 + \frac{1}{\sqrt{\lambda_p}}\right)^{-1} \tag{46}$$

For example, for $\lambda_p=0.5$ and H/W=0.5 it results L=96.6 m. The condition of constant λ_p implies for L2 different lengths of roads as H/W changes. Since the view factors are heavily dependent on the wall length, by comparing the UCs with different lengths, a question arises on the comparability of the view factors for the three simulations. In order to ensure this, in L2 we maintain for H/W=1 and 1.5 the same canyon length as for

H/W=0.5. At the same time, in the heat flow calculation attention is paid to consider the equivalent roof surface that would ensure the maintenance of λ_p=0.5. It is noteworthy that even if the λ_p value is kept constant, the same could not be done simultaneously for the integrated frontal area index λ_f (defined as in [4]). In this study particular attention is given to λ_p, since the roughness length z_0 and the displacement height d_0, which appear in Eq. (12), are strongly dependent on λ_p. Nevertheless, since for urban energy applications the building surface-to-volume ratio (which is a function of both λ_p and λ_f) is a relevant parameter (see for example [45]), further studies should be done to assess the impact of both indices on the schemes sensitivities.

Each surface of the UC is subdivided into three layers. Their thickness and thermal characteristics are listed in Table 1. The initial building temperature (for all layers) is set equal to the external air temperature. To simulate the presence of internal climatization, the internal building air temperature is set to not exceed 23 °C in summer and to not fall below 20 °C in winter.

Table 1. Thermal parameters for roofs, walls and roads used in in the simulations. The layers of the surfaces constituting the UC are indicated by "el" (external layer), by "ml" (middle layer) and by "il" (internal layer). d is the layer thick (m), C the thermal capacity (M $Jm^{-3}K^{-1}$), λ the thermal conductivity (W $m^{-1}K^{-1}$), α the surface albedo and ε the surface emissivity.

	Roof el	*Roof ml*	*Roof il*	*Road el*	*Road ml*	*Road il*	*Wall el*	*Wall ml*	*Wall il*
λ	0.98	0.98	1.51	0.82	2.10	0.40	1.51	0.60	1.51
C	2.10	1.60	2.01	1.70	2.00	1.40	2.01	1.20	2.01
d	0.057	0.27	0.02	0.05	0.20	1.00	0.02	0.26	0.02
α	0.20	-	-	0.10	-	-	0.25	-	-
ε	0.90	-	-	0.95	-	-	0.85	-	-

5. Results

Since L2 is composed of three elements, to compare the results obtained by the three canyons schemes, a spatial averaging of the variables corresponding to the crossroad and the two canyons is calculated. Moreover, as the simulations for L1 and L2 have been conducted for four azimuthal orientations, an additional averaging is performed. However, as expected, the result of averaging over the orientations is that L1 and L0 do not differ between them. This does not mean that L0 and L1 are equivalent. In fact, for an arbitrary canyon orientation, L1 distributes the incident solar energy on both UC walls, and calculates the shadowing more precisely than L0. Figure 5b shows an example of the

daily temperature variation of both UC walls modelled with L0 and L1, considering for the latter a canyon orientation of θ=45°. As expected, the wall temperatures obtained by L0 fails to capture peaks as done by L1. Therefore, in the case of cities with preferred orientation of the roads, the differences between L0 and L1 have to be taken into consideration to interpret the results.

Figs. 6a and 6b show the energy fluxes simulated by L2 in correspondence with the grid node placed at the center of the urban strip for H/W=1. Both in summer (Fig. 6a) and winter (Fig. 6b) the net radiation Q* shows values similar to those obtained by [46] by applying a canopy model for the city of Rome. The sensible heat flux Q_H remains positive all day long and reaches a maximum at noon of about 370 W m^{-2} in summer and 120 W m^{-2} in winter.

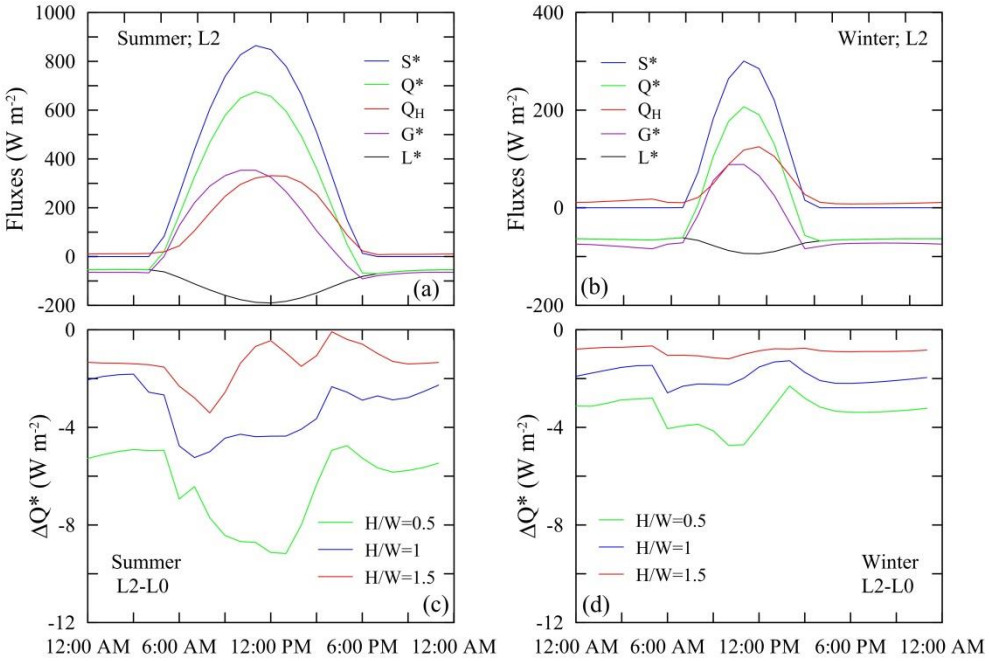

Fig. 6 (a) Daily variations of the surface energy fluxes in summer using L2 with aspect ratio H/W=1 (S*: net shortwave radiation; L*: net longwave radiation; Q*: net radiation; Q_H: sensible heat flux; G*: canopy storage heat flux). (b) As in a), but in winter. (c) Daily variations of the net radiation difference ΔQ^* between L2 and L0 in summer for three H/W. (d) As in c), but in winter.

The heat storage G^* reaches a positive maximum near 10 AM comparable with that attained by Q_H and becomes negative in the early afternoon, similarly to what was observed by [47] and [20]. Similar considerations hold for the energy fluxes simulated in

winter, even though the values are generally lower. Of note, in winter G^* is negative for a large part of the day and reaches negative values of order -100 W m^{-2}.

The disparities between L0 and L2 are quantified by the differences ΔQ^* between the simulated net radiations for the three H/W (summer: Fig. 6c; winter: Fig. 6d). The comparative analysis is particular useful since it makes it possible to distinguish the extent of energy forcing involved in the surface energy balance. Fig. 6c shows that L2 simulates a lower Q^* than L0, especially for H/W=0.5 and in the central part of day, when the net radiation difference exceeds -8 W m^{-2}. In winter (Fig. 6d) ΔQ^* shows smaller values by virtue of the lower solar forcing. It is worthwhile noting the oscillations of ΔQ^* with time associated to the different shadowing simulated by the two schemes.

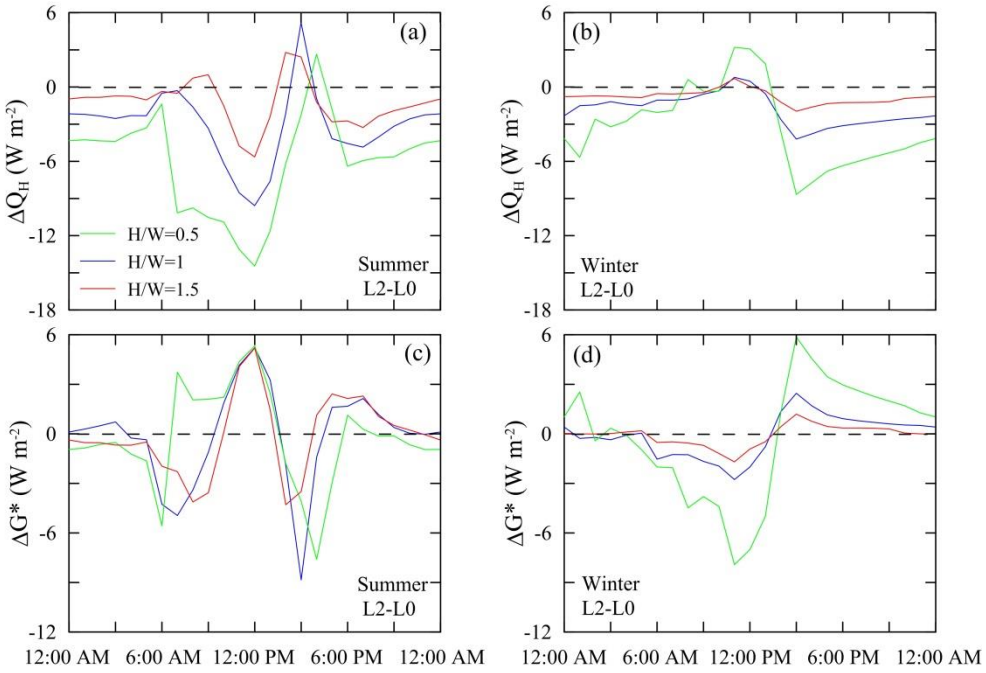

Fig. 7 (a) Daily variation of the sensible heat flux difference ΔQ_H between L2 and L0 in summer for different H/W. (b) As in a), but for the winter. (c) Daily variations of the heat storage flux difference ΔG^* between L2 and L0 in summer for different aspect ratios H/W. (d) As in c), but for the winter.

The differences of the sensible heat fluxes ΔQ_H between L2 and L0 for the three H/W, are depicted in Fig. 7a (summer) and in Fig. 7b (winter). L2 simulates generally lower Q_H than L0 during the day, particularly for H/W=0.5, where the difference reaches -15 Wm^{-2}. This is less visible for H/W=1.5, where the two Q_H are quite similar. Nighttime ΔQ_H remains constant, reaching the value of -5 Wm^{-2} for H/W=0.5. As expected, ΔQ_H for

H/W=1 shows an intermediate trend with respect to the other H/W. Concerning the winter simulations, the differences ΔQ_H for the three aspect ratios are less noticeable with respect to what happens for the summer.

With regard to the heat storages, Fig. 7c shows ΔG^* between L2-L0 calculated in summer for the three H/W. G^* calculated by L2 is, on average and irrespective of H/W, slightly lower than that calculated with L0 as a consequence of the larger sky view factors that increase the infrared radiation outgoing. However, during the central hours of the day the differences fluctuate around zero. Similar considerations are valid for the winter season (Fig. 7d), even though the fluctuations are smaller in amplitude and perceptible only for H/W=0.5. As for the other energy fluxes, the higher ΔG^* occurs for H/W=0.5.

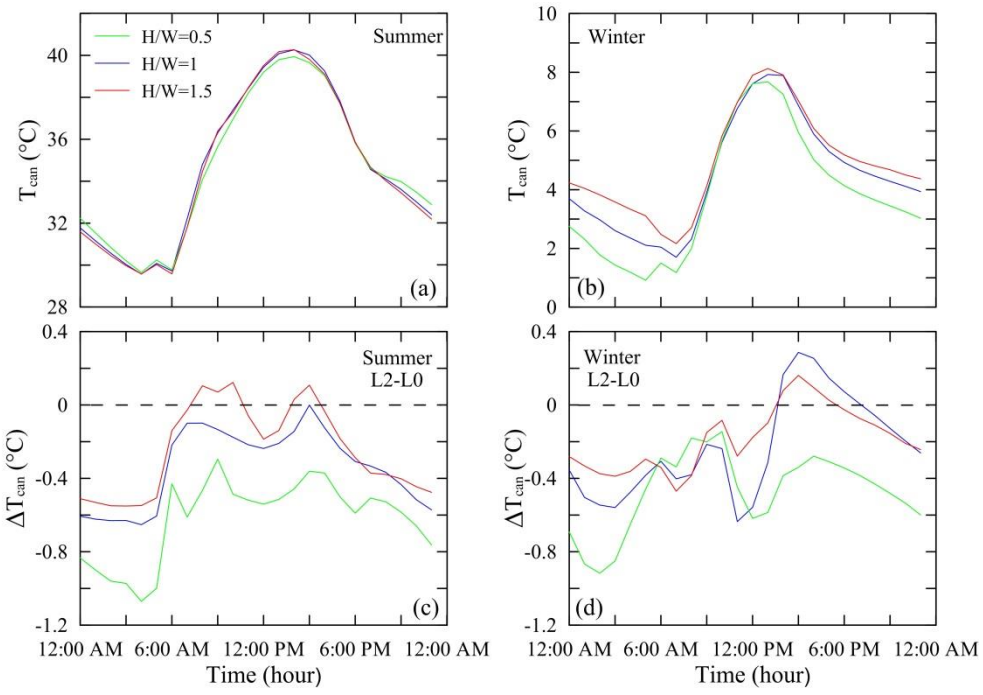

Fig. 8 (a) Daily variations of the air canyon temperature T_{can} for L2 in summer for different H/W. (b) As in a), but for the winter. (c) Daily variations of the air canyon temperature difference ΔT_{can} between L2 and L0 in summer for different H/W (d) As in c), but for the winter.

Figures 8a and 8b show the canyon air temperature T_{can} calculated by L2 in summer and in winter, respectively. The major differences between the three H/W occur at night. In winter, due to the lower solar forcing, a significant role in the energy budget is exerted by the radiative trapping and by the view factors. A consequence is the smaller T_{can}

occurring for H/W=0.5 (Fig. 8b). In contrast, in summer (Fig. 8a) there is an opposite behaviour to that observed in winter for the same H/W as a result of the importance of the effect of shading.

The differences ΔT_{can} between L2-L0 for the summer and the winter cases are reported in Figs. 8c and 8d, respectively. In summer the major ΔT_{can}, of the order of -1 °C occurs during the night. These differences are significantly lower during the day in contrast to what occurs for Q_H. As seen above, the most marked difference takes place for the lower H/W. In winter, ΔT_{can} assumes negative values with the exception of the central hours of the day. The previous analysis suggests that the differences occurring between the canyon schemes are associated mainly to the different value of the view factors as a result of the explicit treatment of the edge effects. In particular, the view factors for L2 assume greater values than those for L0 due to the crossroads. This produces (especially at night) a greater cooling of roads and walls which directly affects T_{can}. The latter, in turn, regulates the sensible heat fluxes Q_H exchanged with the overlying atmosphere. Since the differences between the SVF referred to L0 and L2 decreases as H/W increases, a canyon with aspect ratio H/W=1.5 modelled by L2 behaves similarly to that modelled by L0 (by the view factors point of view), in that the infrared radiation escaping from the canyon edges is small. The trends of the differences shown in Figs. 6-8 in the case of H/W=1.5, are a clear sign of that behaviour.

6. Summary and conclusions

The urban canyon scheme TEB (Town Energy Balance, [6]), is used as the reference model (level L0) to analyze in detail the role played by the urban canyon (UC) representation in the surface energy budget. From L0, two new models of increasing complexity, respectively L1 and L2 are developed. The procedure adopted in the analysis is based on the removal of the geometric approximations on which L0 is based. The removal of the average orientation of the UC, leads to the definition of the L1 scheme, while L2 derives from L1 with the additional assumption of UC with finite length (i.e., crossroads are also taken into account in the energy budget). These three schemes are coupled with the prognostic atmospheric model RAMS 6.0 by means of a two-way connection between RAMS, in order to simulate the dynamic response of L0, L1 and L2

for boundary conditions typically observed in the real case. Several runs are conducted in summer and winter time in correspondence to an idealized domain. The results suggest that neglecting the actual UC orientation (L0 scheme) implies higher net radiation and the temperature within the UC. Furthermore, the improvement related to the use of L1 instead of L0 can be important if the city is characterized by roads with preferred orientations, when the different shadowing of the two canyon walls plays a significant role.

The inclusion of the canyon edge (L2 scheme) results in smaller sensible heat fluxes exchanged with the atmosphere compared to L0. This is particularly evident in summer for small aspect ratios. The differences between L2 and L0 are strictly related to the explicit representation of crossroads. Their presence produces greater SVF with respect to L0 which in turn affect the radiative trapping. The lower trapping results in lower surfaces temperature values, especially for UCs with a wider road. For this reason L2 seems to be a useful tool for applications addressed to the urban comfort study, at least for urban geometry similar to that modeled in L2. In fact, the complete geometry description, allows an accurate assessment of the radiative trapping which regulates the interior and exterior temperatures of the buildings.

Furthermore it should be noted that the chosen plan area fraction, λ_p=0.5, is on the high end of the realistic values [48]. A lower value of λ_p (for example 0.25-0.3 as is the case of north american cities) would increase the importance of the canyon fluxes compared to the roof one. This would result in stronger sensitivity of L2 scheme. However, further analyses are necessary in order to analyze in detail the scheme sensitivity to the urban morphometric parameters.

From the point of view of the urban canopy analysis, the geometrical parameters needed to define a city are functions of the adopted scheme. L0 employs the height of the buildings and the aspect ratio of the urban canyon that characterizes the urban area, while L1 requires information regarding the preferred roads orientation (if the urban fabric allows its identification). L2 requires knowledge of the length of the urban canyons and the crossroads surface extension. L2 clearly has a cost, in terms of the required information, higher than that of L0 and L1. This aspect undermines the feasibility of using L2 for practical applications. The simplified version of L2 presented in this paper

reduces this drawback, limiting the required information to: i) the area of the the building roof that runs alongside the urban canyon, ii) its elevation and iii) the area of the road (including the intersection) that delimits the building on two perpendicular sides (Fig. 3b).

Regardless of the complexity of the scheme adopted to describe the urban SEB, the better understanding of the physical processes depending on the urban geometry can be useful for improving the choices made by modelers to include effects of urbanized areas in NWP models.

APPENDIX A

In the four-facet scheme, the reflection coefficients of the solar radiation undergo changes due to the modeling of both walls. Using the same notation adopted by [6], the component of the reflected solar radiation is:

$$R_i(0) = \alpha_i(S_{dir} + S_{dif}), \quad i = 2,3,4$$

The reflected solar radiations for the road and the walls after n reflections are

$$R_3(n+1) = \frac{\alpha_3}{2}(1-\psi_3)(R_2(n) + R_4(n))$$

$$R_i(n+1) = \alpha_i\psi_i R_3(n) + \alpha_i(1-2\psi_i)R_j(n), \quad i,j = 2,4 \;\; j \neq i$$

The sum of the n contributions for the different surfaces gives:

$$\sum_{k=0}^{n} R_3(k) = \frac{\alpha_3}{2}(1-\psi_3)\left[\sum_{k=0}^{n-1} R_2(k) + \sum_{k=0}^{n-1} R_4(k)\right] + R_3(0)$$

$$\sum_{k=0}^{n} R_i(k) = \alpha_i\psi_i \sum_{k=0}^{n-1} R_3(k) + \alpha_i(1-2\psi_i)\sum_{k=0}^{n-1} R_j(k) + R_i(0), \quad i,j = 2,4 \;\; j \neq i$$

Solving the geometric system above for an infinite number of reflections, one obtains [29]:

$$\sum_{k=0}^{\infty} R_3(k) = M_3 = \frac{a[R_2(0)(\Xi_3 + \Theta_3) + R_3(0)(\chi + \Upsilon_3 + \Pi_3) + R_4(0)(\Psi_3 + \Lambda_3)]}{\chi}$$

$$\sum_{k=0}^{\infty} R_i(k) = M_i = \frac{[R_2(0)(\Xi_i + \Theta_i) + R_3(0)(\Upsilon_i + \Pi_i) + R_4(0)(\Psi_i + \Lambda_i)]}{\chi}, i = 2,4$$

where:

$\chi = 1 - \left(\frac{\gamma c + abc}{\gamma - abe}\frac{\gamma e + ade}{\gamma - acd}\right)$.

$a = \frac{\alpha_3}{2}(1 - \psi_3) \qquad b = \alpha_2\psi_2 \qquad c = \alpha_2(1 - 2\psi_2) \qquad d = \alpha_4\psi_4$

$e = \alpha_4(1 - 2\psi_4) \quad \gamma = 1 - \frac{\alpha_3}{2}(1 - \psi_3)(\alpha_2\psi_2 - \alpha_4\psi_4) = 1 - a(b - d)$

$$\Theta_i = \begin{cases} \frac{\gamma + ab}{\gamma - abe}, & i = 2 \\ \frac{\gamma + ab}{\gamma - abe}\left(1 + \frac{\gamma e + ade}{\gamma - acd}\right), & i = 3 \\ \frac{\gamma + ab}{\gamma - abe}\frac{\gamma e + ade}{\gamma - acd}, & i = 4 \end{cases} \qquad \Lambda_i = \begin{cases} \frac{ab}{\gamma - abe}, & i = 2 \\ \frac{ab}{\gamma - abe}\left(1 + \frac{\gamma e + ade}{\gamma - acd}\right), & i = 3 \\ \frac{ab}{\gamma - abe}\frac{\gamma e + ade}{\gamma - acd}, & i = 4 \end{cases}$$

$$\Xi_i = \begin{cases} \frac{ad}{\gamma - acd}\frac{\gamma c + abc}{\gamma - abe}, & i = 2 \\ \frac{ad}{\gamma - acd}\left(1 + \frac{\gamma c + abc}{\gamma - abe}\right), & i = 3 \\ \frac{ad}{\gamma - acd}, & i = 4 \end{cases} \qquad \Pi_i = \begin{cases} \frac{b}{\gamma - abe}, & i = 2 \\ \frac{b}{\gamma - abe}\left(1 + \frac{\gamma e + ade}{\gamma - acd}\right), & i = 3 \\ \frac{b}{\gamma - abe}\frac{\gamma e + ade}{\gamma - acd}, & i = 4 \end{cases}$$

$$\Upsilon_i = \begin{cases} \frac{d}{\gamma - acd}\frac{\gamma c + abc}{\gamma - abe}, & i = 2 \\ \frac{d}{\gamma - acd}\left(1 + \frac{\gamma c + abc}{\gamma - abe}\right), & i = 3 \\ \frac{d}{\gamma - acd}, & i = 4 \end{cases} \qquad \Psi_i = \begin{cases} \frac{\gamma + ad}{\gamma - acd}\frac{\gamma c + abc}{\gamma - abe}, & i = 2 \\ \frac{\gamma + ad}{\gamma - acd}\left(1 + \frac{\gamma c + abc}{\gamma - abe}\right), & i = 3 \\ \frac{\gamma + ad}{\gamma - acd}, & i = 4 \end{cases}$$

APPENDIX B

The analytical expression of C has been obtained by the polynomial interpolation of the original law reported in [39], viz.:

$$C = a \ln\left(\frac{z_0}{\delta_0}\right) + b \ln\left(\frac{z_0}{\delta_0}\right)^2 + c \ln\left(\frac{z_0}{\delta_0}\right)^{-1} + d \ln\left(\frac{z_0}{\delta_0}\right)^{-2} + e$$

where a=0.01643, b=4.399e-4, c=-1.741, d=-0.1722 and e=0.4128.

APPENDIX C

In comparing the results obtained using the three UC schemes, the different geometry characterizing L2 with respect to the other two schemes should be born in mind. In fact, the presence of the crossroads modeled in L2 results in a greater extension of the road

surface with respect to L1 and L0. Therefore, despite the aspect ratio is the same for the three schemes, a condition of non-comparability occurs. It is therefore of primary importance to set the condition of geometric equivalence:

$$\lambda_p^{L0} = \lambda_p^{L1} = \lambda_p^{L2} = \lambda_p \quad \text{(C1)}$$

where $\lambda_p = A_b/(A_b + A_r)$, while A_b and A_r are the roof top and the street surfaces, respectively. By setting a reference value of λ_p, using the simplified version of L2 (see Section 3.3.3) and the assumption of square buildings of side L, Eq. (C1) yields:

$$\lambda_p^{L2} = \lambda_p = \frac{L^2}{L^2+W^2} \quad \text{(C2)}$$

Equation (C2) can be rewritten as:

$$L^2(1-\lambda_p) - 2w\lambda_p L - \lambda_p W^2 = 0 \quad \text{(C3)}$$

which has two distinct solutions:

$$L = W\left[\frac{\lambda_p}{1-\lambda_p} \pm \frac{\sqrt{\lambda_p}}{1-\lambda_p}\right]$$

Since only the positive solution gives L>0 for $\lambda_p \in]0,1[$, one has:

$$L = W\left(-1 + \frac{1}{\sqrt{\lambda_p}}\right)^{-1} \quad \text{(C4)}$$

which coincides with Eq. (46). This makes it possible to define the size of the building, so that, for a given road width W, the value of λ_p is retained.

References

[1] Fernando HJS, Zajic D, Di Sabatino S, Dimitrova R, Hedquist B, Dallman A (2010) Flow, turbulence, and pollutant dispersion in urban atmospheres. Phys Fluids 22:051301.

[2] Monti P, Leuzzi G (2005) A numerical study of mesoscale airflow and dispersion over coastal complex terrain. Int J Environ Pollut 25:239-250.

[3] Pelliccioni A, Monti P, Gariazzo C, Leuzzi G (2012) Some characteristics of the urban boundary layer above Rome, Italy, and applicability of Monin-Obukhov similarity. Environ Fluid Mech 12:405-428.

[4] Di Sabatino S, Leo LS, Cataldo R, Ratti C, Britter RE (2010) Construction of digital elevations models for a southern European city and a comparative morphological analysis with respect to northern European and north American cities. J Appl Meteorol Climatol 49:1377-1396.

[5] Masson V (2006) Urban surface modeling and the meso-scale impact of cities. Theor Appl Climatol 84(1):35–45.
[6] Masson V (2000) A physically-based scheme for the urban energy budget in atmospheric models Bound-Lay Meteorol 94:357–397.
[7] Kusaka H, Kondo H, Kikegawa Y, Kimura F (2001) A simple single-layer urban canopy model for atmospheric models: Comparison with multi-layer and slab models. Bound-Lay Meteorol 101:329-358.
[8] Dupont S, Mestayer G (2006) Parameterization of the urban budget with the submesoscale soil model. J Appl Meteorol Climatol 45:1744-1765.
[9] Lee S-H, Park S-U (2008) A vegetated urban canopy model for meteorological and environmental modeling. Bound-Lay Meteorol 126:73-102.
[10] Ryu YH, Baik JJ, Lee SH (2011) A new single-layer urban canopy model for use in mesoscale atmospheric models. J Appl Meteorol Climatol 50:1773:1794.
[11] Ca VT, Asaeda T, Ashie Y (1999) Development of a numerical model for the evaluation of the urban thermal environment. J Wind Eng Ind Aerod 81:181-196.
[12] Martilli A, Clappier A, Rotach MW (2002) An urban surface exchange parameterisation for mesoscale models. Bound-Lay Meteorol 104:261–304.
[13] Otte TL, Lacser A, Dupont S, Ching JKS (2004) Implementation of an urban canopy parameterization in a mesoscale meteorological model. J Appl Meteorol 43:1648-1665.
[14] Kondo H, Genchi Y, Kikegawa Y, Ohashi Y, Yoshikado H, Komiyama H (2005) Development of a multi-layer urban canopy model for the analysis of energy consumption in a big city: Structure of the urban canopy model and its basic performance. Bound-Lay Meteorol 116:395-421.
[15] Schubert S, Grossman-Clarke S, Martilli A (2012) A double-canyon radiation scheme for multi-layer urban canopy models. Bound-Lay Meteorol 145:439-468.
[16] Miao S, Li P, Wang X (2009) Building morphological characteristics and their effect on the wind in Beijing. Adv Atmos Sci 26:1115-1124.
[17] Chen F, Pielke Sr RA, Mitchell K (2001) Development and application of land-surface models for mesoscale atmospheric models: Problems and promises. In Land-Surface Hydrology, Meteorology, and climate: Observation and Modeling Water Science and Application Vol.3:107-135.
[18] Holt T, Pullen J (2007) Urban canopy modeling of the New York City metropolitan area: A comparison and validation of single- and multilayer parameterizations (2007) Mon Weather Rev 135:1906-1930.
[19] Masson V, Grimmond CSB, Oke TR (2002) Evaluation of the Town Energy Balance (TEB) scheme with direct measurements from dry districts in two cities. J appl Meteorol 41:1011-1026.
[20] Lemonsu A, Grimmond CSB, Masson V (2004) Modelling the surface energy balance of the core of an old Mediterranean city: Marseille. J Appl Meteorol 43: 312–27.

[21] Lemonsu A, Belair S, Mailhot J, Leroier S (2010) Evaluation of the Town Energy Balance model in cold and snowy conditions during the Montreal Urban Snow Experiment 2005. J Appl Meteorol Climatol 49:346-362.
[22] Freitas ED, Rozoff CM, Cotton WR, Dias PLS (2007) Interactions of an urban heat island and sea-breeze circulations during winter over the metropolitan area of São Paulo, Brazil. Bound-Lay Meteorol 122:43–65.
[23] Rozoff CM, Cotton WR, Adegoke JO (2003) Simulation of St. Louis, Missouri, land use impacts on thunderstorms. J Appl Meteorol 42(6):716–738.
[24] Lei M, Niyogi D, Kishtawal C, Pielke RA, Beltrán-Przekurat A, Nobis TE, Vaidya SS (2008). Effect of explicit urban land surface representation on the simulation of the 26 July 2005 heavy rain event over Mumbai, India. Atmos Chem Phys Discuss 8: 8773–8816.
[25] Cantelli A, Monti P, Leuzzi G (2011) An investigation of the urban heat island of Rome through a canyon-based subgrid scheme. Int J Environ Pollut 47, Nos. 1/2/3/4:239-247.
[26] Porson A, Harman IN, Bohnenstengel SI, Belcher SE (2009) How Many Facets are Needed to Represent the Surface Energy Balance of an Urban Area? Bound-Lay Meteorol 132(1):107–128.
[27] Amicarelli A, Leuzzi G, Monti P, Thomson DJ (2011) LAGFLUM, a stationary 3D Lagrangian stochastic numerical micromixing model for concentration fluctuations: validation in canopy turbulence, on the MUST wind tunnel experiment. Int J Environ Pollut 47, Nos 1/2/3/4:317-325.
[28] Leuzzi G, Amicarelli A, Monti P, Thomson DJ (2012) A 3D Lagrangian micromixing dispersion model LAGFLUM and its validation with a wind tunnel experiment. Atmos Environ 54:117-126.
[29] Cantelli A (2012) Analisi dell'impatto della disomogeneità del tessuto urbano, sulla modellazione dell'isola urbana di calore, mediante uno schema parametrico di sottogriglia. PhD Thesis, Biblioteca Nazionale Centrale di Firenze, Archivio Regionale del Lazio.
[30] Roth M (2000) Review of atmospheric turbulence over cities. Q J R Meteorol Soc 126(564):941–990.
[31] Rotach MW (2001) Simulation of urban-scale dispersion using a Lagrangian stochastic dispersion model Bound-Lay Meteorol 99(3):379–410.
[32] Kastner-Klein P, Rotach MW (2004) Mean flow and turbulence characteristics in an urban roughness sublayer. Bound-Lay Meteorol 111:55–84.
[33] Dyer AJ (1974) A review of flux-profile relationships. Bound-Lay Meteorol 7:363–372.
[34] De Ridder KK (2010) Bulk transfer relations for the roughness sublayer. Bound-lay Meteorol 134:257–267.
[35] Garratt JR (1994) The Atmospheric Boundary Layer. Cambridge University Press, Cambridge.
[36] Mölder M, Grelle A, Lindroth A, Halldin S (1999) Flux-profile relationships over a boreal forest–roughness sublayer corrections. Agricult Forest Meteorol 98:645–658.
[37] Yang K, Tamai N, Koike T (2001) Analytical solution of surface layer similarity equation. J Appl Meteorol 40(9):1647–1653

[38] Harman IN, Barlow JF, Belcher SE (2004) Scalar fluxes from urban street canyons part II: model. Bound-Lay Meteorol 113: 387–410.
[39] Soulhac L, Perkins RJ, Salizzoni P (2008) Flow in a street canyon for any external wind direction Bound-Layer Meteorol 126(3): 365–388.
[40] Oke TR (1987) Boundary layer climates. Routledge, 1987.
[41] Johnson GT, Watson ID (1984) The determination of view-factors in urban canyons. J Appl Meteorol 23:329–335.
[42] Steyn DG, Lyons TJ (1985) Comments on the determination of view factors in urban canyons. J Clim Appl Meteorol 24 (4):383–385.
[43] Cotton WR, Pielke Sr RA, Walko RL et al (2003) RAMS 2001: Current status and future directions. Meteorol Atmos Phys 82:5–29.
[44] Walko RL, Band LE, Baron J, Kittel TGF, Lammers R, Lee TJ, Ojima D, Pielke Sr RA, Taylor C, Tague C, et al. (2000) Coupled atmosphere-biophysics-hydrology models for environmental modeling. J Appl Meteorol 39(6):931–944.
[45] Ratti C, Baker N, Steemers K (2005) Energy consumption and urban texture. Energy and Buildings 37(7):762–776.
[46] Bonacquisti V, Casale GR, Palmieri S, Siani AM (2006) A canopy layer model and its application to Rome. Sci Total Environ 364:1-13.
[47] Piringer M, Joffre S, Baklanov A, Christen A, Deserti M, De Ridder K, Emeis S, Mestayer P, Tombrou M, Middleton D, et al (2007) The surface energy balance and the mixing height in urban areas—activities and recommendations of cost-action 715. Bound-Lay Meteorol 124(1):3–24.
[48] Grimmond CSB, Oke TR (1999) Aerodynamic Properties of Urban Areas Derived from Analysis of Surface Form. J Appl Meteorol 38:1262–1292.